RESEARCH ARTICLE

Rising Stars

ADVANCED OPTICAL MATERIALS

www.advopticalmat.de

Self-Degradable Photoactive Micromotors for Inactivation of Resistant Bacteria

*Xiaojiao Yuan, Salvio Suárez-García, Marco De Corato, Andrés Camilo Muñoz, Ignacio Pagonabarraga, Daniel Ruiz-Molina, and Katherine Villa**

Pathogenic bacteria pose a significant threat to human health, and their removal from food and water supplies is crucial in preventing the spread of waterborne and foodborne diseases. Recently, silver-based photocatalytic micromotors have emerged as promising candidates for inactivating pathogenic microbes due to their high antibacterial activity. In this study, the synthesis of photoactive Ag_3PO_4 micromotors with a well-defined tetrapod-like structure (TAMs) is presented using a simple precipitation method. These TAMs autonomously move and release Ag ions/nanoparticles (NPs) through a photodegradation process when exposed to light, which enhances their antimicrobial activity against Gram-negative (*Escherichia coli*) and Gram-positive (*Staphylococcus aureus*) bacterial strains. Interestingly, different motion modes are observed under different manipulated light wavelengths and fuels. Furthermore, the self-degradation of TAMs is accelerated in the presence of negatively charged bacteria, which results in higher removal rates of both bacteria, *E. Coli* and *S. aureus*. The findings introduce a new concept of self-degradable micromotors based on photocatalytic components, which hold great potential for their use in antimicrobial applications. This work offers significant implications for materials chemistry, especially in designing and developing the next generation of light-driven antimicrobial agents.

1. Introduction

Photoactive self-propelled micro/nanoscale motors exhibit great promise for various applications, due to their remote control, reversible on/off motion, and tunable light wavelength manipulation by alternating their chemical and optical composition.[1] Mainstream semiconductors such as UV light-responsive nano/micromotors based on TiO_2,[2] ZnO,[3] AgCl[4] and visible light active materials, such as Cu_2O,[5] $BiVO_4$,[6] porous donor-acceptor polymers[7] and C_3N_4[8] have been widely investigated. The ability of such photoactivated micromotors to release reactive radicals under light irradiation has triggered their potential application in the environmental field for the removal of organic pollutants, heavy metals, and pathogenic microorganisms. In the latter, mainly TiO_2,[9] ZnO,[10] and silver-based micromotors have been used for antimicrobial applications. Unfortunately, these micromotors are only photoactive in the UV light range and/or require toxic chemical fuels and surfactants to activate their self- propulsion, which limits their applicability under real conditions.[11] In particular, silver-based micromotors are well-known for their strong biocidal effects.[12] For instance, AgCl microstar-shaped micromotors were used to remove *E. coli*.[13] However, their activity was attributed to the silver component and not the photocatalytic activity since both performances under dark and UV irradiation were similar. Recently, visible-light responsive Ag_3PO_4 micromotors[14] have garnered

X. Yuan, A. C. Muñoz, K. Villa
Institute of Chemical Research of Catalonia (ICIQ)
The Barcelona Institute of Science and Technology (BIST)
Av. Països Catalans, 16, Tarragona E-43007, Spain
E-mail: k.villa@iciq.es

S. Suárez-García, D. Ruiz-Molina
Catalan Institute of Nanoscience and Nanotechnology (ICN2)
CSIC and BIST
Campus UAB, Bellaterra, Barcelona 08193, Spain

M. De Corato
Department of Science and Technology of Materials and Fluids, Fluid Dynamics Technology Group (TFD), Aragon Institute of Engineering Research (I3A)
University of Zaragoza
María de Luna, 3, Zaragoza 50018, Spain

I. Pagonabarraga
Departament de Física de la Matèria Condensada
Universitat de Barcelona
Carrer de Martí i Franqués 1, Barcelona 08028, Spain

I. Pagonabarraga
Universitat de Barcelona Institute of Complex Systems (UBICS)
Universitat de Barcelona
Barcelona 08028, Spain

The ORCID identification number(s) for the author(s) of this article can be found under https://doi.org/10.1002/adom.202303137

DOI: 10.1002/adom.202303137

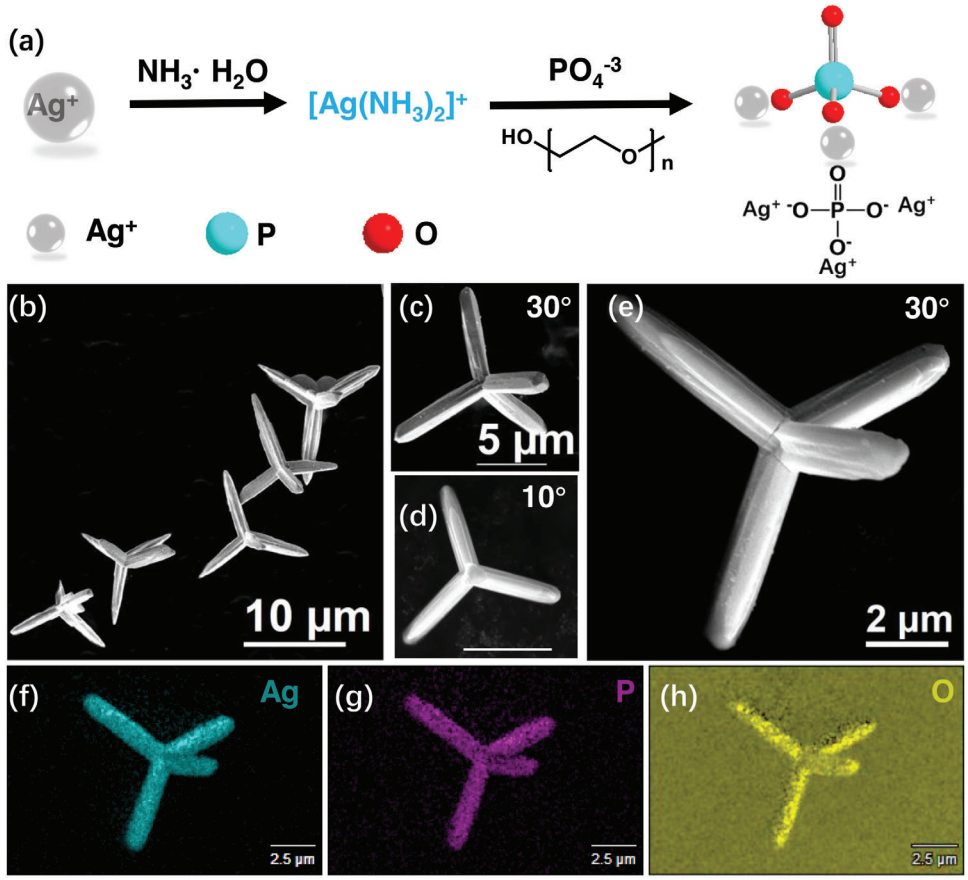

Figure 1. Fabrication and characterization of TAMs. a) Schematic illustration showing the synthesis procedure of TAMs. b–e) FESEM images of TAMs, including different tilting angles. f–h) energy dispersive X-ray (EDS) mapping images that show the Ag, P, and O distribution.

attention from various groups. For instance, Sen et al. studied the collective behaviors of Ag_3PO_4 micromotors made of an amorphous morphology.[4c,15] Moreover, Rojas et al. investigated the influence of amorphous, cubic and pyramidal shapes of Ag_3PO_4 on their motion efficiencies, resulting in overall low motion performances.[14] While these micromotors have been used for biofilm removal, their interactions with released Ag ions, planktonic cells, as well as their stability under light irradiation in different liquid media, remain largely unexplored. On the other hand, Ag_3PO_4 with defined crystal facets have shown improved photocatalytic performance for degradation of pollutants, due to the availability of more surface active sites.[16]

Here, we introduce tetrapod-shaped Ag_3PO_4 micromotors capable of generating high shear forces under visible light illumination that enhance their propulsion in a fluid environment. This unique morphology was obtained by a simple precipitation method with a reaction between $[Ag(NH_3)_2]^+$ complex and Na_2HPO_4 without the need of additional surfactants. Moreover, these TAMs exhibit fast motion velocity not only in water but also in biocompatible fuels, such as glucose. By manipulating the light wavelength of light and fuels, the TAMs exhibit tunable propulsion modes, including rotational and linear locomotion. Moreover, we studied the antimicrobial activity of TAMs against both planktonic Gram-positive and Gram-negative bacteria and the respective biofilms under visible light irradiation (λ = 500 nm). Interestingly, we found out that the micromotors self-degrade very quickly (less than 1 min) in the presence of bacteria, resulting in a rapid release of Ag NPs that effectively kill the bacteria. Overall, this work demonstrates a new approach for developing efficient photocatalytic micromotors with high antibacterial activity that disaggregate under light irradiation, making them a promising alternative for environmental remediation. It also sheds light on the interactions between photocatalytic micromotors and bacteria that opens up new avenues for exploring the relationship between structure, motion, and biological activities.

2. Results and Discussion

2.1. Fabrication of TAMs

TAMs were fabricated by a facile precipitation method, as illustrated in **Figure 1a**. In brief, an aqueous solution of $AgNO_3$ was mixed with $NH_3{\cdot}H_2O$ to form a $[Ag(NH_3)_2]^+$ complex that serves as an intermediate compound to form the TAMs in the presence of Na_2HPO_4 solution (see the Experimental Section). The ammonia acts as a coordination agent that slows down the reaction rate, while the phosphate ions bind to the Ag_3PO_4 (110) surface, leading to the formation of the tetrapod morphology.[17] The morphological properties of TAMs were investigated by using field emission scanning electron microscope (FESEM). The composition

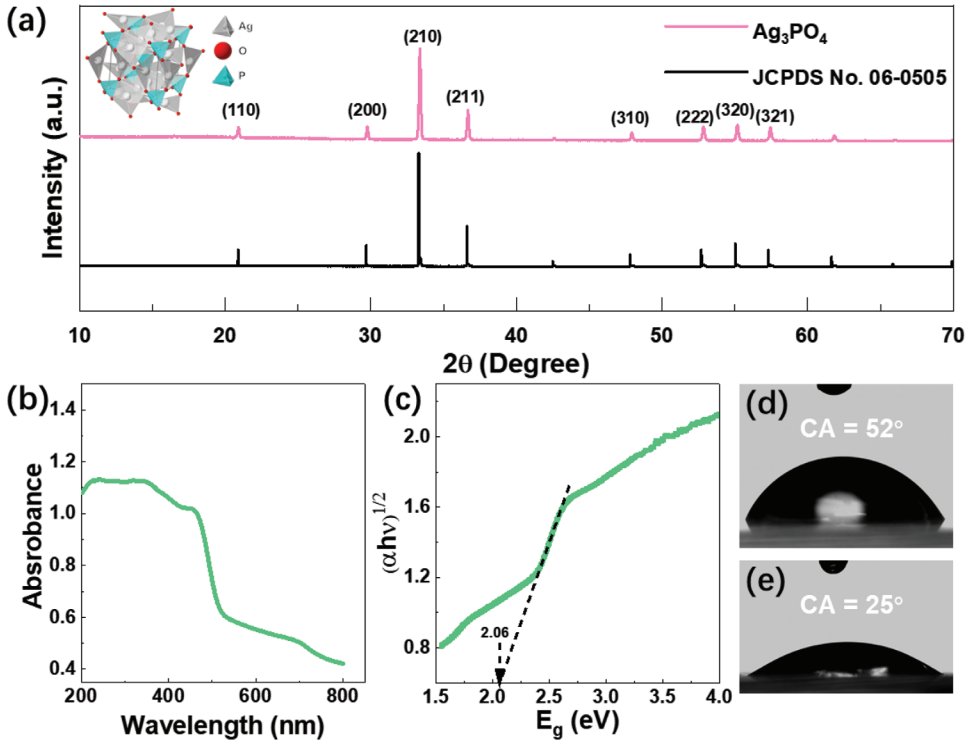

Figure 2. Structural and optical characterization of TAMs. a) XRD pattern of TAMs. b) UV–vis spectrum of TAMs and c) calculated optical bandgap of TAMs by Tauc plot. d) Contact angle of glass and e) TAMs film on glass in presence of water.

of Ag_3PO_4 can be described as tetrapodal microcrystals with a 3D structure (Figure 1b–e; Figure S1, Supporting Information). The average size of TAMs was calculated from FESEM images of a minimum of ten particles, and it was found to be 4 ± 0.5 µm. EDS analysis confirms the elemental components of the TAMs, including Ag, P, and O elements (Figure 1f–h).

The crystalline structure of TAMs was characterized by X-ray powder diffraction (XRD). **Figure** 2a shows that the XRD diffraction peaks of the micromotors are in agreement with the standard value of normal cubic phase Ag_3PO_4 (JCPDS No. 06–0505) with no impure phases detected.[18] Additionally, the UV–vis absorption spectrum of TAMs is included in Figure 2b. Moreover, a bandgap of 2.06 eV was determined by Tauc plots (indirect bandgap) (Figure 2c), which is much smaller than that of reported tetrahedra, rhombic dodecahedra, and cubic Ag_3PO_4 particles.[19] The excellent visible optical absorption property of the micromotors facilitates the inducement of photochemical reactions in the visible range of the solar spectrum. Other factors such as the wettability of the surface and the surrounding fluid can also have a significant impact on the performance of the micromotors because of the surface tension or capillary forces to operate.[20] As shown in Figure 2d,e, TAMs present good hydrophilicity in water (contact angle CA = 25°), which facilitates the motion and increases the biocompatibility of micromotors. Besides, the surface charge of TAMs also plays an important role in bacterial removal applications. Figure S2 (Supporting Information) represents the zeta potential values of TAMs, which exhibit a positive surface charge. As a result, it leads to an electrostatic attraction with the negatively charged bacterial cell walls, increasing the chances of a higher contact between the micromotors and the bacterial surface.

2.2. Motion Characterization of TAMs

The motion trajectories of single-component micromotors are greatly affected by their morphologies and external factors such as overlapping gradients from neighboring particles and photogenerated chemical gradient around the particle. The motion capabilities of TAMs were evaluated in pure water and glucose under UV and visible light irradiation. **Figure** 3a and Figure S3 (Supporting Information) show the screenshots of the circular motion trajectories of TAMs under visible and UV light irradiation in pure water, respectively (Videos S1 and S2, Supporting Information). The motion of TAMs in glucose (Figure S4, Supporting Information) under visible and UV light irradiation is included in Videos S3 and S4 (Supporting Information), respectively. In general, two types of motion behaviors were observed, varying from rotational to linear motion directions. However, since it was not observed a homogeneous trend under each specific light wavelength, such differences in their motion modes might be related to defects in their morphology that affect the local flow generated around the micromotors instead of the wavelength light source.[21]

As can be seen from Figure 3b, TAMs can reach similar speeds under UV or blue light irradiation for the different chemical environments, showing, in any case, the highest velocity of ≈8.0 µm s^{-1} in the presence of glucose under UV light irradiation

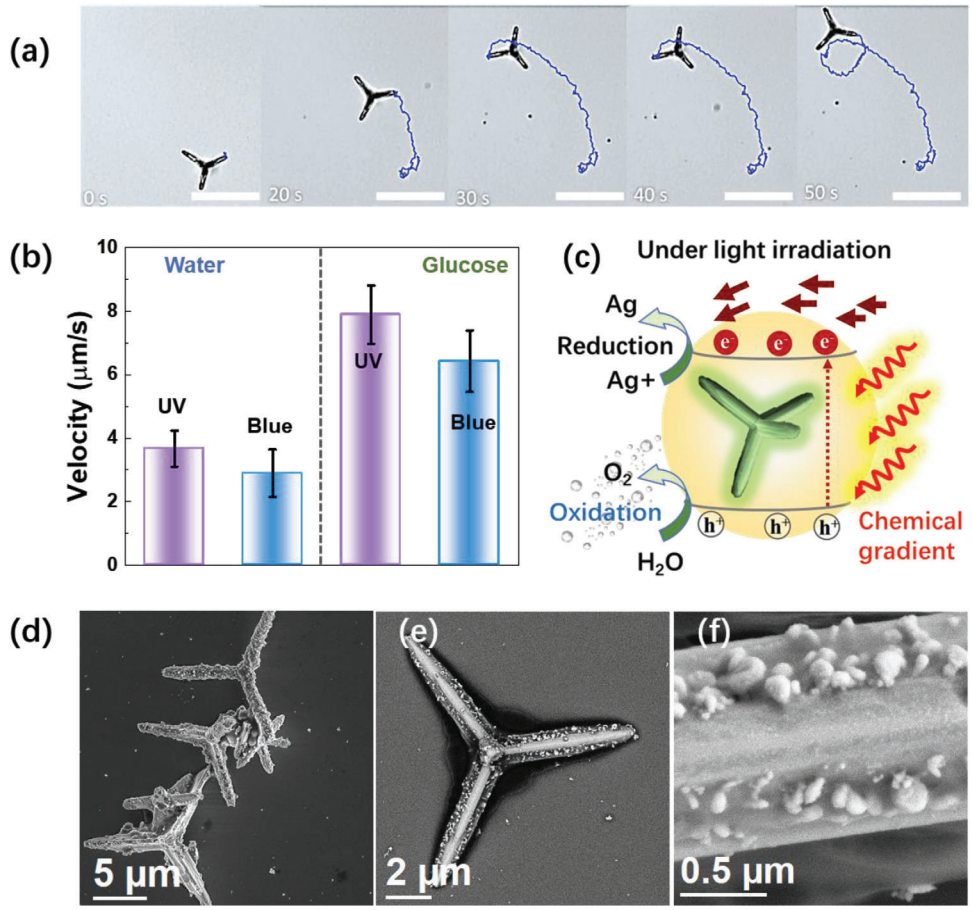

Figure 3. Motion characterization of TAMs. a) Motion trajectories of TAMs in pure water under blue light (scale bar: 10 μm). b) Speeds of TAMs in the presence of different solutions under UV and blue light, respectively (the bars represent the mean and the error represent the standard deviation of the mean; $n = 15$). c) Proposed photocatalytic motion mechanism of TAMs. d–f) FESEM images of TAMs in the presence of glucose after 10 min of UV light irradiation.

(6.4 μm s^{-1} under blue light irradiation). Such values are comparable to other types of photocatalytic micromotors based on short-bandgap materials, such as Cu_2O.[22]

The motion mechanism can be explained by considering the photocatalytic behavior of TAMs (Figure 3c). Upon irradiation, electrons in the valence band (VB) are promoted to the conduction band (CB). The photogenerated holes react with water or glucose, leading to the formation of O_2 or carbon-based intermediates,[22] respectively. Meanwhile, the photogenerated electrons reduce the released Ag^+ ions into Ag NPs, leading to the self-photoreduction of Ag_3PO_4, as shown in Equation (1).[16a] Since these photogenerated ions diffuse at different rates, it drives the motion of TAMs by self-diffusiophoresis.[16b] Considering that visible-light-responsive TAMs can be efficiently activated in the presence of glucose, it offers a promising alternative to enzyme-catalyzed glucose oxidation.[22,23]

$$4Ag_3PO_4 + 6H_2O \rightarrow 4Ag + 8Ag^+ + O_2 + 4OH^- + 4H_2PO_4^- \quad (1)$$

Given that the releasement of Ag^+ ions by Ag_3PO_4 under light irradiation might affect its stability,[24] we further studied the motion behavior of the micromotors under a long-term irradiation in the presence of different fuels. We observed that TAMs release Ag NPs while moving in the surroundings. A faster self-photodegradation process was observed in the presence of glucose in comparison to water. This can be attributed to the fact that this fuel acts as a hole scavenger, enhancing the availability of photogenerated electrons that participate in the reduction of the photogenerated Ag^+ ions into Ag NPs.

Additionally, we collected liquid samples in the presence of TAMs under both dark and light conditions. Prior to analysis, the solid was removed by centrifugation and the liquid samples were further analyzed by inductively coupled plasma mass spectrometry (ICP-MS) measurements. As can be seen from Table S1 (Supporting Information), TAMs release silver under both conditions, with significantly higher levels detected after irradiation. We also performed FESEM characterization of TAMs following prolonged irradiation. Figure 3d–f illustrates the surface etching of TAMs after 10 min of light irradiation in the presence of glucose.

Similar behaviors were observed in water, where released Ag particle sizes ranged between 0.2–0.6 μm (Figure S5, Supporting Information). Despite the self-reduction process, the structural and chemical properties were maintained, as confirmed by XRD

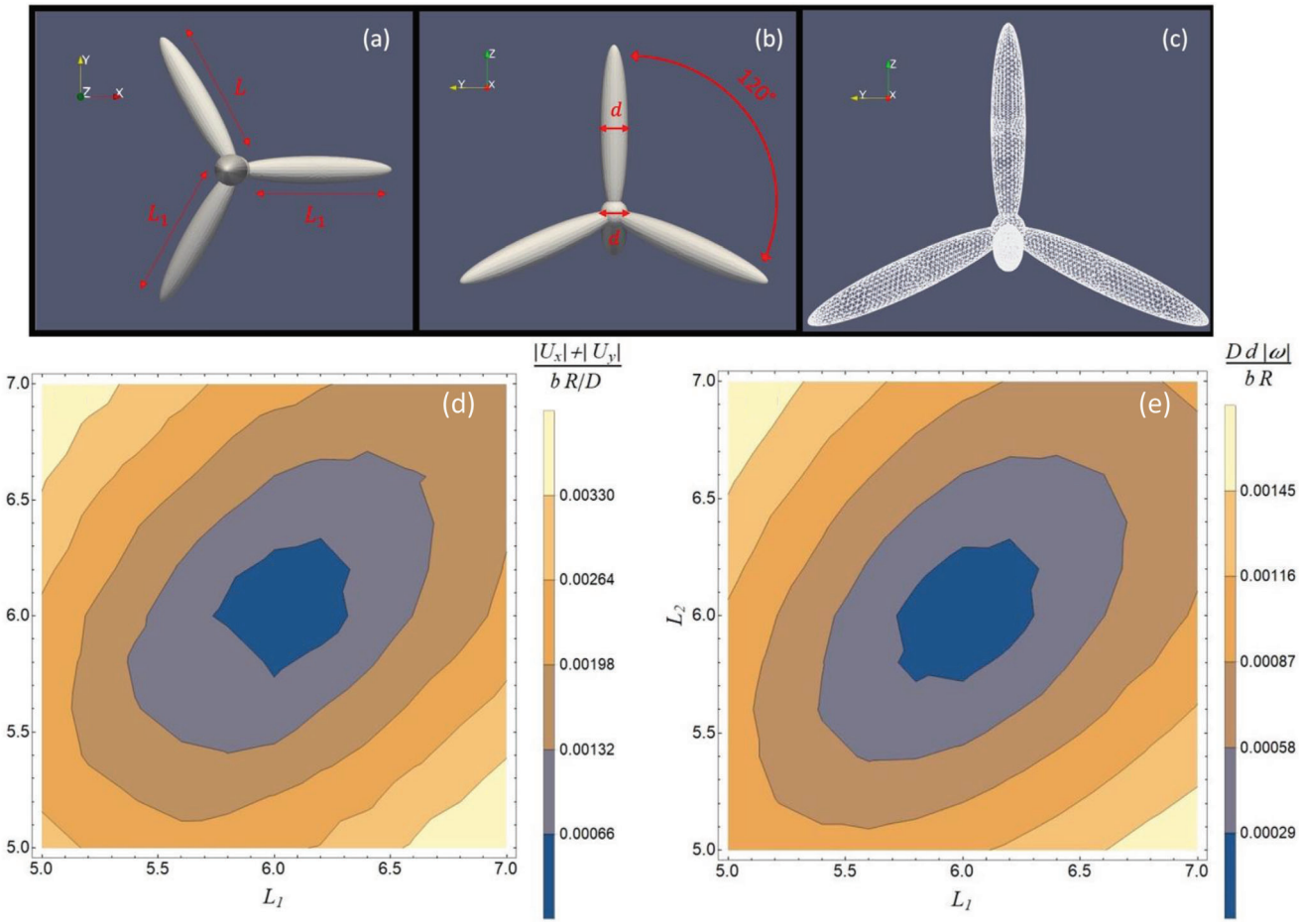

Figure 4. Numerical simulations of TAMs. a,b) Characteristic lengths and angles of the geometry used in the simulations to model the tetrapod. Here we show the symmetric case $L_1 = L_2 = L$. c) surface mesh that is used to discretize the surface. d) Dimensionless magnitude of the translational velocity component projected on the x-y plane and e) Dimensionless magnitude of the angular velocity as a function of the length L_1 and L_2 of the tetrapod legs. If $L_1 \neq L_2 \neq L$ the symmetry of the particle is broken, and the tetrapod acquires a translational and rotational velocity.

and Fourier-transform infrared spectroscopy (FTIR) characterization before and after irradiation (Figures S6 and S7, Supporting Information).

Complementarily, we performed numerical simulations using the finite element method to understand the origin of the motion. For this purpose, we considered a tetrapod consisting of four ellipsoids of major axis, L, and minor axis, *d*, that are oriented along the four vertices of a tetrahedron with the addition of a sphere of diameter, *d*, placed at the center (**Figure** 4a,b). To match the geometrical proportions of the tetrapod used in the experiments, we choose $d = 1$ μm and $L = 6$ μm. Since a tetrahedron is symmetric under rotation around the z-axis, translations in the x-y plane and rotations around any of the axes are forbidden by symmetry. However, we show here that motion and rotation can occur if two of the ellipsoids forming the legs of the tetrahedron display a different length $L_1 \neq L_2 \neq L$.

We assume that the reactive species produced during the reaction interact with the surface of the tetrapod driving a diffusiophoretic flow over a small length-scale of the size of the Debye layer. Since the reaction involves charged reactants and products, which greatly complicates a detailed analysis,[25] we simplified the model by assuming that only one of the product species interacts with the surface and drives the diffusiophoretic surface flow. This allows us to simulate only one concentration field, which we denote with *c*. Since the velocity of the motor is small, we neglect the transport of species due to advection. It follows that the product species, *c*, satisfies the diffusion Equations (2) and (3):

$$D\,\Delta c = 0 \tag{2}$$

With D the diffusion coefficient of the reactive species and Δ denotes the Laplacian operator. The product species is produced at a rate $R(x)$ on the reactive part of the surface, where x is the coordinate of a point on the surface of the tetrapod:

$$-D\,\nabla c \cdot n = R\,(x) \tag{3}$$

In the experiments, the surface catalytic activity is driven by irradiation with light from below and directed vertically, i.e., along the z-axis in Figure 4. As a result, it is reasonable to assume that the reaction rate decreases along the z coordinate. We model this by choosing $R(x) = R$ on the lower surface of the ellipsoid

forming the legs and R(x) = 0 on the remaining surface of the tetrapod. The reactive portion of the particle is shown as the yellow surface in Figure S8 (Supporting Information), while the inactive portion is shown in purple.

We assume that the concentration of the product is zero at infinity, which is a good approximation, at least at the beginning of the reaction. In the computational model, the boundary condition, $c = 0$, at infinity is placed on a sphere with a radius $r =$ 300 μm, which is much larger than the size of the tetrapod. Using a larger domain with $r = 500$ μm gave indistinguishable results. The computational domain is discretized into tetrahedral elements that are smaller near the tetrapod and become larger as the distance from the surface increases. Figure 4c gives an example of the elements of the mesh on the boundary of the tetrapod.

The gradients of product species drive surface flows, v_s, proportional to the diffusiophoretic coefficient, b,

$$v_s = b\nabla_{\|}c \tag{4}$$

where $\nabla_{\|}$ is the gradient operator along the surface of the tetrapod defined as $\nabla_{\|} = \nabla \cdot (I - nn)$, with I the identity tensor. The diffusiophoretic coefficient, b, depends on the details of the interaction between the product and the surface of the tetrapod and the viscosity of the liquid.[26] Here, we treat b as an unknown parameter.

The fluid flow around the tetrapod satisfies the Stokes flow Equations (5) and (6)

$$\eta\,\Delta v - \nabla p = 0 \tag{5}$$

$$\nabla \cdot v = 0 \tag{6}$$

With η the shear viscosity of the liquid. The translational and rotational velocity of the tetrapod are then computed using the force-free and torque-free conditions (Equations (7) and (8))

$$\int_S n \cdot \sigma \, \mathrm{d}S = 0 \tag{7}$$

$$\int_S r \times (n \cdot \sigma) \, \mathrm{d}S = 0 \tag{8}$$

where S is the surface of the tetrapod, r is the distance vector of any point of the surface from the center of the tetrapod and σ is the Cauchy stress tensor given by Equation (9)

$$\sigma = \frac{\eta}{2}\left(\nabla v + \nabla v^T\right) - p\, I \tag{9}$$

We used cubic elements that are used to discretize the concentration field and the velocity field and quadratic elements to discretize the pressure field. We first solve the concentration field and then use the diffusiophoretic velocity to solve the Stokes problem. The resulting linear systems are solved using an iterative solver.

The solution to the Equations (2)–(9) yields the kinematics of the tetrapod for different lengths of the two legs of the tetrapod, L_1 and L_2. In Figure 4d, we report the contour plot of the magnitude of the projection of the translational velocity on the x-y plane, rescaled by b R/D. In Figure 4e we report the magnitude of the angular velocity, rescaled by D d/b R. Since the governing equations are linear, the dimensionless translational velocity and rotational velocity depend on the geometry of the tetrapod only. Figure 4d,e shows that, if the length of the legs of the tetrapod, L_1 and L_2 are different from L, then the active particle acquires a translational and a rotational velocity. This result is consistent with the experimental observation that the length of the legs of the tetrapod change in time as the chemical reaction consumes the tetrapod. Indeed, our simulations show that the translational and rotational velocities are the largest when the three legs have different length, $L_1 \neq L_2 \neq L$. In summary, the numerical results suggest that the geometrical asymmetry of the tetrapod generated by the chemical reaction is responsible for the trajectory observed in the experiments.

We further conducted a study to investigate the motion and stability of TAMs under acidic and basic pH conditions. The micromotors were not stable in highly acidic environments (pH 3.5) as most of them were already broken apart. However, this effect was less significant at a basic pH of ≈10. The reason for these different behaviors may be attributed to a lack of chemical stability of Ag_3PO_4 in such acidic media and/or the reduced availability of photogenerated holes under acidic conditions compared to a basic environment.[27] Consequently, there is a greater amount of photogenerated electrons that convert Ag^+ ions into metallic Ag.[28]

2.3. Antimicrobial Activity of TAMs

By taking advantage of the active motion of TAMs and the simultaneous release of Ag ions/NPs under light irradiation, we further investigated the antibacterial activity of these micromotors against pathogenic microorganisms (**Figure 5a**). We selected *E. coli* and *S. aureus* as representatives of Gram-negative and Gram-positive bacteria, respectively. Initially, our focus was on studying the interactions and motion behaviors of the TAMs in the presence of bacteria. Surprisingly, we observed that the micromotors self-degrade much faster in the presence of both types of bacteria (Video S5, Supporting Information). A complete self-degradation times of TAMs were generally 35 s and 60 s in the presence of *E. Coli* and *S. aureus*, respectively (Figure 5b,c). This results in a higher availability of Ag NPs in the liquid media (Video S6, Supporting Information).

Additionally, we investigated the bactericidal activity of TAMs in water under blue irradiation by fluorescence microscopy. Propidium iodide (PI) was used as a fluorescent probe to identify dead cells, indicated by a red fluorescent color (Figure 5d).[29] As can be seen from Figure 5e, in the absence of light, only a few dead *E. Coli* cells were observed. However, upon activation of TAMs under visible light, nearly all *E. Coli* cells exhibited a red fluorescent color, proving the high photoactivity of the micromotors after a brief period of light exposure. Such antibacterial effect can be attributed to the ability of TAMs to generate highly oxidizing reactive oxygen species (ROS) during photocatalytic process, along with the release of silver (Ag NPs/Ag^+ ions) into the surrounding media, which disrupt the cell membrane of microorganisms.[23,30]

Complementarily, we validated the antibacterial activity of TAMs by the colony-forming units (CFU) method. To accomplish

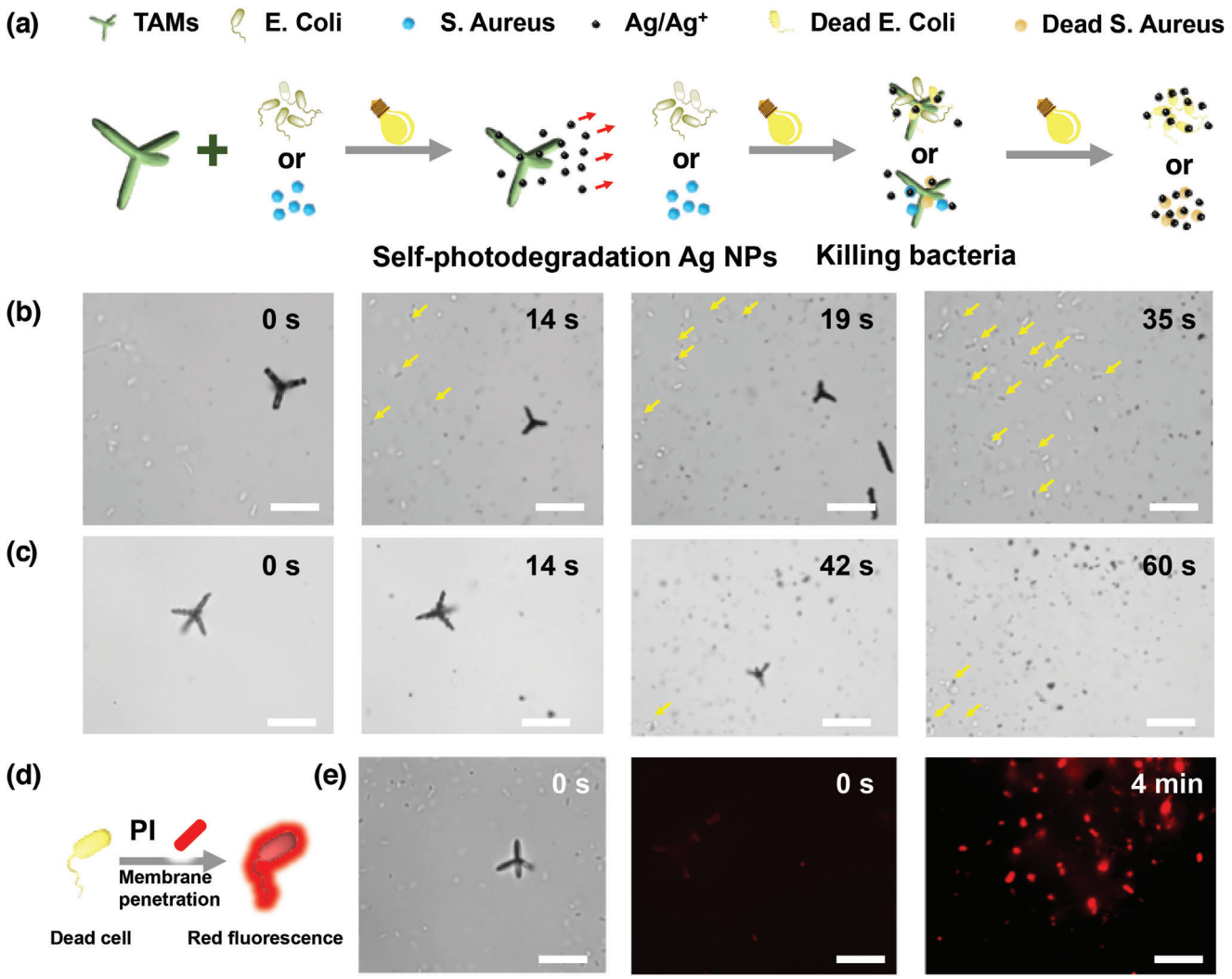

Figure 5. Interactions of TAMs and bacteria under light irradiation. a) Schematic illustration of the interaction with bacteria. b) Photodegradation evolution of TAMs over time in the presence of *E. coli* and c) *S. aureus* under light irradiation; Yellow arrows point to bacteria that are being attacked by Ag NPs. d,e) Fluorescence microscopy images showing the antibacterial activity of TAMs against *E. coli*. Scale bar: 10 µm.

this, we assessed the logarithmic reduction of CFU in the presence of the micromotors under both dark and visible light irradiation, using the single plate-serial dilution spotting (SP-SDS) assay with *E. coli* and *S. aureus*. Briefly, the micromotors at different concentrations (0.01, 0.05, 0.1, 0.5, and 1 mg mL^{-1}) were incubated for 5 and 30 min for each bacteria strain, under both light and dark conditions. When the micromotors were incubated with *E. coli* and irradiated with light (λ = 500 nm) for 5 min, we observed a CFU log reduction of ≈−2.5 (**Figure** 6a). Interestingly, the antibacterial efficacy decreased when the incubation was performed under dark conditions, suggesting a beneficial effect of light exposure on the mobility of the micromotors and their enhanced interaction with bacteria. With longer incubation times (30 min), we observed higher CFU log reduction in both light and dark conditions, albeit with a higher antibacterial effect when exposed to light. SEM images show the direct contact between TAMs and bacteria and the released Ag NPs on the surface of dead bacteria after irradiation, which further demonstrates their high affinity on the surface of TAMs (Figure 6b). Similar trends were observed with *S. aureus* (Figure 6c,d), showing even increased antibacterial efficiency (CFU log reduction of ≈−3.1 for 5 min of incubation), probably because the lack of an outer membrane in Gram-positive bacteria, which weakens their barrier against damage. On the contrary, Gram-negative bacteria possess an outer membrane that provides resistance to alterations in hydrophobic properties or oxidative stress, making them more resilient to antibiotics.

Overall, the incubation with two different bacteria strains revealed an antibacterial activity of the micromotors above 99.999% when irradiated with light and incubated for 30 min. Furthermore, among the different concentrations tested, it was found that 0.05 mg mL^{-1} was enough to observe a drastic reduction in the bacteria populations (Figures S9–S11, Supporting Information). The enhanced antibacterial activity of TAMs under light irradiation may be attributed to their self-propulsion and an increased availability and dispersion of Ag NPs due to the

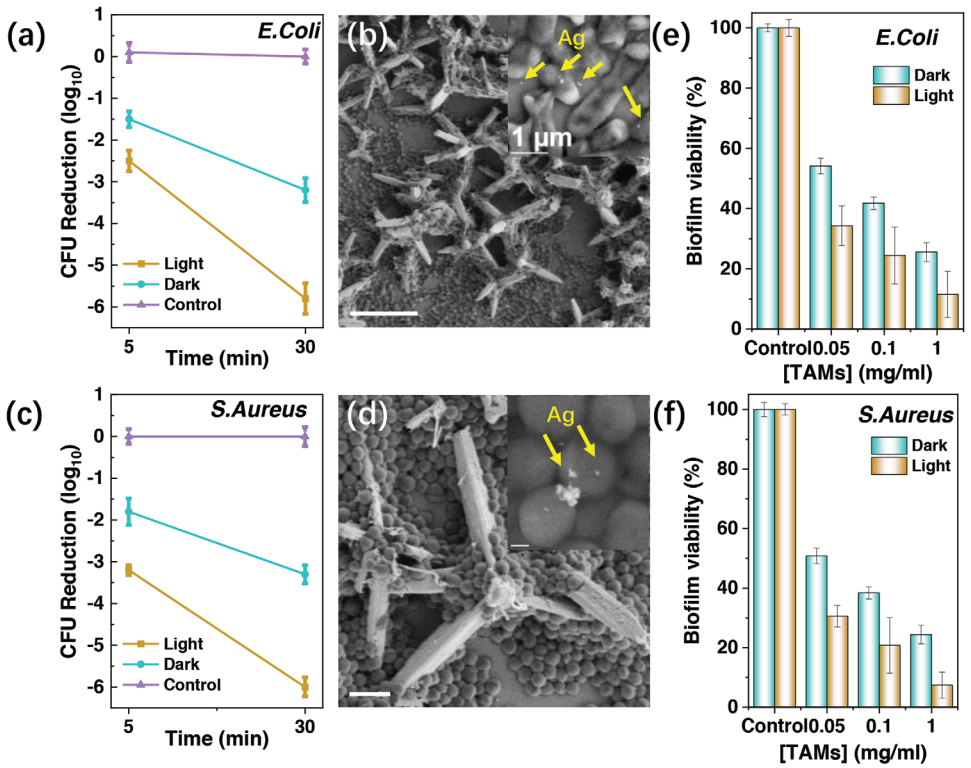

Figure 6. Antibacterial activity of TAMs. a) Colony-forming unit (CFU) logarithmic reduction of *E. coli* under dark and visible light (λ = 500 nm) and without TAMs (control). The error bars represent the standard deviation of the mean; n = 5. b) SEM images of TAMs in the presence of *E. Coli* after 30 min reaction under visible light irradiation. c) Colony-forming unit (CFU) logarithmic reduction of *S. aureus* under dark and visible light (λ = 500 nm) and without TAMs (control). The error bars represent the standard deviation of the mean; n = 5. d) SEM images of TAMs in the presence of *S. aureus* after 30 min reaction under visible light irradiation. e) *E. Coli* and f) *S. aureus* biofilm treated with TAMs under dark and visible-light exposure conditions for 60 min and three different concentrations (0.05, 05, and 1 mg mL^{-1}). The bars represent the mean and the error represents the standard deviation of the mean; n = 6.

self-photodegradation process occurring as they move within the liquid media.

To further validate the enhanced antibacterial properties attributed to the self-propulsion and photocatalytic activity of TAMs induced by light irradiation, two additional experiments were performed. In the first experiment, Ag NPs at a concentration of 1 mg mL^{-1} were incubated for 5 and 30 min against *E. coli* and *S. aureus* strains, under both light and dark conditions. The results showed a CFU log reduction of ≈−1.3 and −2.9 for 5 min and 30 min of incubation, respectively (Figure S12, Supporting Information). Notably, this reduction was less than half when compared with the efficacy of TAMs. Furthermore, exposure to light did not exhibit any positive effect on the bactericidal capacity of Ag NPs. These findings suggest that the antibacterial efficiency of TAMs cannot solely be attributed to the release of Ag NPs or ions. Instead, the self-propulsion of TAMs facilitates enhanced interactions with bacteria, thereby avoiding their propagation more effectively.

To shed more light in this phenomenon, a second experiment was performed involving the immobilization of TAMs on a glass surface. In this experiment, TAMs at a concentration of 1 mg mL^{-1} were drop casted on top of glass substrate, dried and subsequently inoculated with both *E. coli* and *S. aureus* strains. Interestingly, when irradiated with light, the immobilization of TAMs considerably diminish their antibacterial capacity. Specifically, a CFU log reduction of ≈−1 and −0.5 was observed for 30 and 5 min, respectively (Figure S13, Supporting Information). Comparatively, in previous experiments where TAMs were freely moving in suspension at the same concentration, the CFU log reduction reached values of ≈−6 and −3 for 30 min and 5 min, respectively. Overall, these results demonstrate the essential role of the TAMs motion to endow the system with more efficient antibacterial capacity.

In addition to studying planktonic cells, we further evaluated the capabilities of TAMs for biofilm eradication using two different bacterial biofilms (*E. coli* and *S. aureus*). The biofilm viability assay was performed under dark and light exposure at three different concentrations (0.05, 05, and 1 mg mL^{-1}). As shown in Figure 6e, the presence of TAMs dramatically affected *E. Coli*-based biofilm viability, which was highly decreased in dark conditions (with a reduction of 46%, 58%, and 74% for 0.05, 05, and 1 mg mL^{-1} of TAMs, respectively). Moreover, biofilm viability decreased even further under light exposure (with a reduction of 66%, 76%, and 89% for the concentrations of TAMs of 0.05, 05, and 1 mg mL^{-1}, respectively).

Similar trends were observed for *S. aureus*-based biofilm, with a high viability decrease of the biofilm under both dark and light conditions (Figure 6f). Specifically, under dark conditions, biofilm viability decreased by 50%, 62%, and 76% for concentrations of TAMs of 0.05, 05, and 1 mg mL^{-1} of TAMs,

respectively. Under light exposure, these reductions were even more pronounced, with a reduction of 69%, 79%, and 93% for the respective concentration of TAMs of 0.05, 05, and 1 mg mL^{-1}, respectively. Consistent with previous findings, TAMs were more effective under light conditions with higher antibacterial activity when incubated with *S. aureus*. The biofilm eradication was further confirmed through fluorescence imaging, which revealed a reduction in biofilm intensity with increasing concentrations of TAMs (Figure S14, Supporting Information).

The excellent antibacterial properties shown by the TAMs can be explained through multifaceted mechanisms. As has been previously reported, Ag-based nanomaterials have the ability to efficiently kill microorganisms through the interaction with the cell membranes, where the Ag^+ ions in the bacteria surroundings can damage its permeability by generating surface tension, therefore inducing high lateral stress. Such stress causes irreversible membrane damage and its subsequent death, leading to leakage of cell contents.[31] Besides, the penetration of Ag^+ ions into the cytoplasm promotes the disruption of several cellular functions over the denaturation of the bacterial proteins and by forming complexes with nucleic acids, causing the interruption of DNA replication.[32] Among these mechanisms, the photocatalytic properties of TAMs play an essential role in inactivating pathogens by the production of ROS under visible light irradiation.[33] In this regard, we conducted tests to measure the photogeneration of ROS by TAMs, evidencing the production of H_2O_2, $O_2^{\bullet-}$, and $^{\bullet}OH$ radicals (Figure S15, Supporting Information).

Moreover, the antibacterial properties can be enhanced by the specific features of the micromotors. In this sense, the hydrophilicity and the positive surface charge of TAMs substantially contributed to the bacteria damage. Hydrophilicity facilitates the efficient dispersion of TAMs in water-based media, where bacteria typically thrive, thereby enhancing interactions at the biointerface. Moreover, the positively charged surface of TAMs promotes their accumulation in the vicinity of negatively charged bacteria due to attractive forces. This accumulation translates into higher antibacterial efficiency and better dispersion of bactericidal agents. It is worth noting that all the mechanisms discussed previously are potentially enhanced by the autonomous movement of TAMs, providing significant advantages in breaking through biological barriers. This motion allows for accelerating ion penetration and physical damage of bacterial cell walls and biofilms.

3. Conclusion

In conclusion, we have successfully fabricated tetrapod-like Ag_3PO_4 micromotors via a simple precipitation method without the use of surfactants. The unique tetrapod structure of TAMs confers efficient motion propulsion in the presence of biocompatible fuels under visible light irradiation. Interestingly, these micromotors exhibited a tunable motion mode and excellent on/off characteristics achieved by alternating light sources and chemical environments. Moreover, these photoactive micromotors showed remarkable antibacterial activity against two bacterial strains for both planktonic and biofilms, achieving a reduction of bacterial population above 99.999% and 89% decrease when exposed to visible light and incubated for 30 min, respectively. The high bactericidal capabilities of TAMs were attributed to their active motion and self-degradation with the concomitant release of Ag ions/NPs and ROS under light-irradiation. A significant reduction in bacterial population and biofilm removal was obtained at a concentration of 0.05 and 1 mg mL^{-1}, respectively, evidencing the potential of these devices for water purification. These results highlight the structure-propulsion-activity relationships for bacterial removal, which provides a new vision to design photoactive micromotors for biological and environmental applications with self-degradable abilities.

4. Experimental Section

Reagents: Silver nitrate ($AgNO_3$), ammonia solution (28–30% analysis), sodium phosphate monobasic dihydrate ($NaH_2PO_4{\cdot}_2H_2O$), and poly-ethylene glycol (PEG-400) were purchased from Sigma-Aldrich. Deionized water (Milli-Q, 18.6 MΩ) was used throughout all experiments.

Synthesis of TAMs: TAMs were synthesized by a facile precipitation method as described as follows: First, $AgNO_3$ (0.1 g) was dissolved in water (6 mL) and $NH_3{\cdot}H_2O$ (168 µL) to form solution 1. Then, Na_2HPO_4 (4.44 g) was dissolved in water (43 mL) and PEG-400 (6 g) to form solution 2. Then, solution 1 was dropwise added into solution 2 under stirring (400 rmp) at 60 °C for 1 h (Figure 1a). Finally, the light-green powder was collected by centrifugation, washed, and dried.

Characterization of TAMs: The surface morphology of the TAMS was characterized by high-resolution FESEM with a focused ion beam (Ga) (FESEM-FIB, Zeiss Supra 35 at 5 kV, 25 pA), and the chemical analysis of the films was performed on a FESEM Inspect F50 with EDAX. UV–vis diffuse reflectance spectrometer (DRS) (Agilent Cary 60) with a wavelength range of 200–800 nm was used to collect absorption spectra. XRD was obtained with a Bruker AXS D8-Discover diffractometer (40 kV and 40 mA). The zeta potential values of the powder samples suspended in water were measured using a ZSNano Zetasizer instrument (ZEN 3600, Malvern). For the contact angle measurements, the TAMs powder (10 mg) was first suspended in water (5 mL) and the resulting suspension was spray coated onto a glass substrate to form the film. Then, the contact angle of the film was measured by Krüss drop shape analyzer DSA 100. The amount of Ag released by the TAMs under dark and light irradiation was quantified by ICP-MS (Agilent 7900). For this purpose, a suspension of TAMs (1 mg mL^{-1}) in water was kept in the dark or under UV–vis light irradiation for 30 min. After this, the TAMs were collected by centrifugation and the amount of the remanent Ag from the liquid samples was measured. The motion speeds of the TAMs were estimated by a FIJI software from the recorded videos using a confocal microscope (Nikon TE 2000E) coupled to a halogen lamp and a Hamamatsu camera.

Bacterial Growth Conditions: *Escherichia coli* (MG1655) and *Staphylococcus aureus* (CECT86) were streaked on a 100 mm petri dish containing Miller's Luria-Bertani (LB) with agar and incubated for 24 h at 37 °C (Forma Series II Water-Jacketed CO_2 Incubator). Bacteria cultures were resuspended in NaCl saline solution 0.9% and the optical density (OD_600) of the suspension was adjusted (Fisherbrand Cell Density Meter Model 40) to 0.2 for *E. coli* and 0.3 for *S. aureus*. All procedures were performed under a laminar flow cabin and sterile techniques.

SP-SDS Methodology: Before testing the antibacterial properties of TAMs, the powder was introduced in 10 mL glass vials and exposed to UV light for 1 h for its sterilization. Then, different concentrations of TAMs (0.01 mg mL^{-1}, 0.05 mg mL^{-1}, 0.1 mg mL^{-1}, 0.5 mg mL^{-1} and 1 mg mL^{-1}) were added to a vial containing each bacteria strain. After obtaining the corresponding OD_600 for each bacteria suspension, 120 µl were inoculated in the vial with the sample. After the desired incubation time (5 and 30 min), dilution −1 was obtained directly with the sample inside the vial. Subsequently, the remaining serial dilutions (−2 to −5) were also performed. Plates were seeded following the already described methodology for SP-SDS[34] and incubated for 24 h at 37 °C. After this time, viable CFUs were read, having a total number of repetitions of N = 5 for each

condition. Experiments with light exposition were performed using a lamp with a 500 nm emission tube (VL6, Vilber Lourmart). Results were represented with OriginPro version 9.8.0.200 software.

Interaction of TAMs with Bacteria: *E. coli* cells were stained with a PI dye. For the optical visualization of the antibacterial effect of TAMs, a suspension of *E. coli* and micromotors (40 µL) was mixed with PI staining dye (1 µL, 0.5 mg mL^{-1}). Time-lapse images were taken with a confocal microscope (Nikon TE 2000E) under light exposure.

Biofilm Experiments: Bacterial cultures of *E. coli* (MG1655) or *S. aureus* (CECT86) were diluted in brain heart infusion broth (BHI) medium to adjust an OD_600 of 0.2. Then 200 µL of bacterial inoculum were pipetted into 96- well plates for 7 days of incubation at 37 °C, changing the medium every day. After incubation, the formed biofilm plates were washed three times with phosphate-buffered saline (PBS). The TAMs were added at different concentrations (0.05, 0.1 and 1 mg mL^{-1}), applying two different conditions: dark and light (irradiating the plate with a lamp) and incubated for 60 min. After incubation, the biofilms were washed three times with PBS. The biofilm viability was evaluated by measuring the fluorescence of each well (560/590 nm, excitation/emission), using alamarBlue staining (ThermoFisher Scientific) following the specifications from the manufacturer. The experiments were performed by doing 6 repetitions for each control and TAMs concentrations. Error bars are expressed as the standard deviation. Controls only with bacteria and in the presence/absence of light (VL6 lamp) were performed. Fluorescent images of the biofilm were obtained using a Zeiss Axio Observer Z1m (Carl Zeiss AG, Jena, Germany) microscope in fluorescence mode and Alexa Fluor 546 filter.

ROS Production Assay: A fluorogenic kit MAK143 (Sigma Aldrich, Merck) was used and applied as indicated by the manufacturer. First, 180 µl of Master-Reaction-Mix (MRM) were mixed with 20 µl of water. Then, the TAMs were added at different concentrations (0.05, 0.1, and 1 mg mL^{-1}). The fluorescence was measured at 5 and 30 min after irradiating with light, keeping a temperature of 25 °C (Varioskan LUX, Thermo Scientific and $\lambda_{excitation}$ = 490 nm/$\lambda_{emission}$ = 525 nm for excitation and emission wavelength, respectively). Three repetitions of each condition were performed.

Supporting Information

Supporting Information is available from the Wiley Online Library or from the author.

Acknowledgements

Project supported by a 2023 Leonardo Grant (RobotsFun) for Researchers and Cultural Creators, BBVA Foundation. The BBVA Foundation accepts no responsibility for the opinions, statements, and contents included in the project and/or the results thereof, which are entirely the responsibility of the authors. This research has also received funding from the European Union (ERC, PhotoSwim, 101076680). Views and opinions expressed are however those of the authors only and do not necessarily reflect those of the European Union or the European Research Council. Neither the European Union nor the granting authority can be held responsible for them. K.V. acknowledges the Ramón y Cajal grant, RYC2021-031075-I funded by MICIU/AEI/10.13039/501100011033 and by the "European Union Next generation EU/PRTR". X.Y. thanks the financial support by "Juan de la Cierva Grant" FJC2021-047222-I, funded by MICIU/AEI/10.13039/501100011033 and by the "European Union NextGenerationEU/PRTR". M.D.C. acknowledges the Ramon y Cajal grant RYC2021-030948-I funded by MICIU/AEI/10.13039/501100011033 and by the "European Union NextGenerationEU/PRTR". I.P. acknowledges support from Ministerio de Ciencia, Innovación y Universidades MICIU/AEI/FEDER for financial support under grant agreement PID2021-126570NB-100 AEI/FEDER-EU, and from Generalitat de Catalunya under Program Icrea Acadèmia and project 2021SGR-673. This work was also supported by grant PID2021-127983OB-C21 funded by MICIU/AEI/10.13039/501100011033 and by ERDF A way of making Europe. The ICN2 was funded by the CERCA programme/Generalitat de Catalunya. The ICN2 was supported by the Severo Ochoa Centres of Excellence programme, Grant CEX2021-001214-S, funded by MICIU/AEI/10.13039.501100011033.

Conflict of Interest

The authors declare no conflict of interest.

Data Availability Statement

The data that support the findings of this study are available in the supplementary material of this article.

Keywords

Ag_3PO_4, antibacterial activity, photoactive micromotors, photocatalysis

Received: December 10, 2023
Revised: February 7, 2024
Published online: March 14, 2024

[1] a) Y. Tu, F. Peng, D. A. Wilson, *Adv. Mater.* **2017**, *29*, 1701970; b) K. Villa, M. Pumera, *Chem. Soc. Rev.* **2019**, *48*, 4966; c) P. Mena-Giraldo, M. Kaur, S. L. Maurizio, G. A. Mandl, J. A. Capobianco, *ACS Appl. Mater. Interfaces* **2024**, *16*, 4249; d) R. Maria-Hormigos, C. C. Mayorga-Martinez, M. Pumera, *Small Methods* **2023**, *7*, 2201014.

[2] a) T. Maric, M. Z. M. Nasir, R. D. Webster, M. Pumera, *Adv. Func. Mater.* **2020**, *30*, 1908614; b) S. Giudicatti, S. M. Marz, L. Soler, A. Madani, M. R. Jorgensen, S. Sanchez, O. G. Schmidt, *J. Mater. Chem. C* **2014**, *2*, 5892; c) R. Dong, Q. Zhang, W. Gao, A. Pei, B. Ren, *ACS Nano* **2016**, *10*, 839; d) M. Urso, L. Bruno, S. Dattilo, S. C. Carroccio, S. Mirabella, *ACS Appl. Mater. Interfaces* **2023**, *16*, 1293; e) Z. Amiri, A. Hasani, F. Abedini, M. Malek, H. R. Madaah Hosseini, *ACS Appl. Mater. Interfaces* **2024**, *16*, 3019.

[3] a) Y. Ying, A. M. Pourrahimi, C. L. Manzanares-Palenzuela, F. Novotny, Z. Sofer, M. Pumera, *Small* **2020**, *16*, 1902944; b) R. Liu, L. Zhao, S. Yang, J. Lin, X. Wang, D. Chen, G. Lu, H. Chen, Z. Wang, Z. Ye, *J. Phys. Chem. C* **2023**, *127*, 12026.

[4] a) X. Wang, L. Baraban, V. R. Misko, F. Nori, T. Huang, G. Cuniberti, J. Fassbender, D. Makarov, *Small* **2018**, *14*, 1802537; b) X. Wang, L. Baraban, A. Nguyen, J. Ge, V. R. Misko, J. Tempere, F. Nori, P. Formanek, T. Huang, G. Cuniberti, *Small* **2018**, *14*, 1803613; c) M. Ibele, T. E. Mallouk, A. Sen, *Angew. Chem.* **2009**, *121*, 3358; d) J. Lin, K. Xiong, J. Hu, Z. Li, L. Xu, J. Guan, *Adv. Intell. Syst.* **2023**, *5*, 2300386.

[5] D. Zhou, Y. C. Li, P. Xu, N. S. McCool, L. Li, W. Wang, T. E. Mallouk, *Nanoscale* **2017**, *9*, 75.

[6] a) K. Villa, F. Novotný, J. Zelenka, M. P. Browne, T. Ruml, M. Pumera, *ACS Nano* **2019**, *13*, 8135; b) Z. Chen, J. Jiang, X. Wang, H. Zhang, B. Song, B. Dong, *J. Mater. Sci.* **2022**, *57*, 4092; c) X. Yuan, R. Ferrer-Campos, F. A. Garcés-Pineda, K. Villa, *Small* **2023**, *19*, 2207303.

[7] Y. S. Kochergin, K. Villa, F. Novotný, J. Plutnar, M. J. Bojdys, M. Pumera, *Adv. Func. Mater.* **2020**, *30*, 2002701.

[8] a) K. Villa, C. L. Manzanares Palenzuela, Z. k. Sofer, S. Matějková, M. Pumera, *ACS Nano* **2018**, *12*, 12482; b) K. Feng, J. Gong, J. Qu, R. Niu, *ACS Appl. Mater. Interfaces* **2022**, *14*, 44271.

[9] J. Li, V. V. Singh, S. Sattayasamitsathit, J. Orozco, K. Kaufmann, R. Dong, W. Gao, B. Jurado-Sanchez, Y. Fedorak, J. Wang, *ACS Nano* **2014**, *8*, 11118.

[10] M. Ussia, M. Urso, K. Dolezelikova, H. Michalkova, V. Adam, M. Pumera, *Adv. Func. Mater.* **2021**, *31*, 2101178.

[11] J. Parmar, D. Vilela, K. Villa, J. Wang, S. Sánchez, *J. Am. Chem. Soc.* **2018**, *140*, 9317.
[12] a) D. Vilela, M. M. Stanton, J. Parmar, S. Sánchez, *ACS Appl. Mater. Interfaces* **2017**, *9*, 22093; b) J. Wang, S. Wu, W. Zhang, H. Wang, P. Zhang, B. Jin, C. Wei, R. Guo, S. Miao, *Appl. Clay Sci.* **2022**, *216*, 106352.
[13] J. Simmchen, A. Baeza, A. Miguel-Lopez, M. M. Stanton, M. Vallet-Regi, D. Ruiz-Molina, S. Sánchez, *ChemNanoMat* **2017**, *3*, 65.
[14] D. Rojas, M. Kuthanova, K. Dolezelikova, M. Pumera, *NPG Asia Mater* **2022**, *14*, 63.
[15] a) A. Altemose, A. J. Harris, A. Sen, *ChemSystemsChem* **2020**, *2*, 1900021; b) A. Altemose, M. A. Sánchez-Farrán, W. Duan, S. Schulz, A. Borhan, V. H. Crespi, A. Sen, *Angew. Chem. Int. Ed.* **2017**, *56*, 7817.
[16] a) Y. Yao, Q. Shen, Q. Chen, Y. He, L. Jiang, J. Liu, Y. Li, X. Cao, H. Yang, *ACS Appli. Nano Mater.* **2024**, *7*, 3711; b) Y. Yao, Q. Shen, C. Wu, C. Lu, J. Sheng, Y. Li, H. Yang, *New J. Chem.* **2023**, *47*, 10497.
[17] a) H. Wang, L. He, L. Wang, P. Hu, L. Guo, X. Han, J. Li, *CrystEngComm* **2012**, *14*, 8342; b) C. Tang, E. Liu, J. Wan, X. Hu, J. Fan, *Appl. Catal. B* **2016**, *181*, 707.
[18] Y. Bi, H. Hu, S. Ouyang, G. Lu, J. Cao, J. Ye, *Chem. Comm.* **2012**, *48*, 3748.
[19] a) M.-S. Hsieh, H.-J. Su, P.-L. Hsieh, Y.-W. Chiang, M. H. Huang, *ACS Appl. Mater. Interfaces* **2017**, *9*, 39086; b) J. Ke, J. Zhao, M. Chi, M. Wang, X. Kong, Q. Chang, W. Zhou, C. Long, J. Zeng, Z. Geng, *Nat. Comm.* **2022**, *13*, 932.
[20] C. Gao, C. Zhou, Z. Lin, M. Yang, Q. He, *ACS Nano* **2019**, *13*, 12758.
[21] Y. Mu, W. Duan, K. Y. Hsu, Z. Wang, W. Xu, Y. Wang, *ACS Appl. Mater. Interfaces* **2022**, *14*, 57113.
[22] Q. Wang, R. Dong, C. Wang, S. Xu, D. Chen, Y. Liang, B. Ren, W. Gao, Y. Cai, *ACS Appl. Mater. Interfaces* **2019**, *11*, 6201.
[23] M. Y. Memar, R. Ghotaslou, M. Samiei, K. Adibkia, *Infect. Drug Resist* **2018**, *11*, 567.
[24] W. Duan, R. Liu, A. Sen, *J. Am. Chem. Soc.* **2013**, *135*, 1280.
[25] a) M. De Corato, X. Arqué, T. Patiño, M. Arroyo, S. Sánchez, I. Pagonabarraga, *Phys. Rev. Lett.* **2020**, *124*, 108001; b) E. S. Asmolov, T. V. Nizkaya, O. I. Vinogradova, *Physics of Fluids* **2022**, *34*, 032011; c) J. L. Moran, J. D. Posner, *Annu. Rev. Fluid Mech.* **2017**, *49*, 511.
[26] J. L. Anderson, *Annu. Rev. Fluid Mech.* **1989**, *21*, 61.
[27] R. Li, X. Song, Y. Huang, Y. Fang, M. Jia, W. Ma, *J. Mol. Catal. A: Chem.* **2016**, *421*, 57.
[28] L. Luo, Y. Li, J. Hou, Y. Yang, *Appl. Surf. Sci.* **2014**, *319*, 332.
[29] V. Juvekar, C. S. Lim, D. J. Lee, S. J. Park, G. O. Song, H. Kang, H. M. Kim, *Chem. Sci.* **2021**, *12*, 427.
[30] M. Quinteros, V. C. Aristizábal, P. R. Dalmasso, M. G. Paraje, P. L. Páez, *Toxicology in vitro* **2016**, *36*, 216.
[31] a) E. P. Ivanova, D. P. Linklater, M. Werner, V. A. Baulin, X. Xu, N. Vrancken, S. Rubanov, E. Hanssen, J. Wandiyanto, V. K. Truong, *Proc. Natl. Acad. Sci* **2020**, *117*, 12598; b) P.-P. Li, H.-X. Wu, A. Dong, *Rare Metals* **2022**, *41*, 519.
[32] M. López-Heras, I. Theodorou, B. Leo, M. Ryan, A. Porter, *Environ. Sci. Nano* **2015**, *2*, 312.
[33] A. Bhattacharyya, R. Chattopadhyay, S. Mitra, S. E. Crowe, *Physiol. Rev.* **2014**, *94*, 329.
[34] M. J. Hajipour, K. M. Fromm, A. A. Ashkarran, D. J. de Aberasturi, I. R. de Larramendi, T. Rojo, V. Serpooshan, W. J. Parak, M. Mahmoudi, *Trends Biotechnol* **2012**, *30*, 499.